Nanoparticles reveal permanent and reversible changes to lymph node biomechanics during inflammatory response

Ann Ramirez[1 #], Vedanth Sriram[1,2 #], Yassmin Abbouchi[1], Reina Patolia[1], Emily Passaro[1], Michele Kaluzienski[1], Katharina Maisel[1,2*]

Affiliations:

1: Fischell Department of Bioengineering, University of Maryland, College Park

2: Biophysics Program, University of Maryland, College Park

#Authors contributed equally to the manuscript

*** Correspondence to:**

Dr. Katharina Maisel

Fischell Department of Bioengineering

University of Maryland, College Park

Email: maiselka@umd.edu

ABSTRACT

Lymph nodes are highly specialized immune organs that orchestrate the adaptive immune response. In the lymph nodes, naïve B and T lymphocytes encounter cognate antigens, sparking their activation and response to foreign substances. Lymph nodes grow in response to an immune challenge, at least in part to accommodate increased numbers of infiltrating and proliferating B and T lymphocytes. This behavior is supported by a robust three-dimensional network of extracellular matrix (ECM) fibers and fibroblastic reticular cells (FRCs). ECM fibers and FRCs work synergistically to alternate stretching and contractile forces between them allowing the lymph node to maintain structural integrity during rapid tissue reconstruction. These changes ultimately alter the material properties of the lymph node, which can impact cell migration, proliferation, and differentiation. Recent work has investigated the physiological implications of the changing lymph node microenvironment; however, the biophysical properties of the lymph nodes during these changes remain largely unexplored. Here, we use multiple particle tracking microrheology (MPT), a minimally invasive nanoparticle-based technique to investigate the biophysical properties (elastic/loss moduli, microviscosity, pore size) of lymph nodes post inflammatory stimulus. Our results highlight mechanical changes both during the initial phases of the acute inflammatory response and upon resolution of inflammation, a topic that is relatively understudied. We show that B and T cell rich areas exhibit comparable changes in biomechanical properties over time, suggesting that they restructure in a similar fashion during acute inflammation.

Additionally, for the first time, we show that biological sex modulates lymph node biomechanics in acute inflammation: Lymph nodes from female mice showed a ~20-fold increase in elastic and loss moduli at peak inflammation, while lymph nodes from male mice had a ~5-fold decrease in both moduli. Additionally, lymph nodes from female mice appeared to permanently remodel

during the resolution of acute inflammation resulting in the maintenance of an overall higher elastic and loss modulus, while lymph nodes from male mice returned to the biomechanics of untreated lymph nodes. We also found that at least some of the changes in biomechanical properties were correlated with changes in ECM materials in the lymph nodes, suggesting a structure-function relationship. Overall, our studies provide key insights into how biomechanical properties in lymph nodes are altered during inflammation, a previously unstudied area, and lay the foundation for structure-function relationships involved in immune response. Additionally, we demonstrate a robust technique for the analysis of the lymph node interstitial tissue properties and how they vary with inflammatory stimuli.

33 **INTRODUCTION**

34 The lymph node is key in shaping the adaptive immune response. The complex
35 coordination of adaptive immune cell (lymphocyte)-mediated immune responses is largely due to
36 the lymph node's highly organized structure. The lymph node can be separated into three distinct
37 regions: the cortex, paracortex, and medulla. The T cell response, the cell-mediated arm of adaptive
38 immunity that results in direct killing of, e.g., infected or cancerous cells, is coordinated in the
39 paracortex. The B cell response, our humoral or antibody-mediated immunity, is coordinated in
40 the cortex. Lymph fluid travelling from peripheral tissues to the lymph nodes flows around the
41 lymph node and into the inner medulla as well as into the subcapsular sinus, and into the cortex
42 and paracortex. Macrophages that line the subcapsular sinuses break down larger materials into
43 smaller antigens to be released into the cortex or paracortex to stimulate T and B cell responses,
44 and small materials <100 kDa in size enter the cortex and paracortex via the conduit system[1]. The
45 conduit system, also called the reticular network, is made up of fibroblastic reticular cells (FRCs)
46 that ensheath a network of collagen fibers that build a key structural component within the lymph
47 node. FRCs maintain these fibers and produce additional collagen during lymph node expansion
48 and contraction that occur during immune responses[2,3]. Other non-lymphocytes, including
49 fibroblasts, blood and lymphatic endothelial cells, as well as macrophages, also contribute to
50 changes in the lymph node structure during inflammation and as we age.

51 During inflammatory processes, the lymph node undergoes significant structural changes.
52 Within a few hours of an immune insult, whether a bacterial infection due to a cut or the onset of
53 a flu infection, a massive influx of migrating lymphocytes and antigen presenting cells, including
54 dendritic cells (DCs) coming from the injured tissue, enter the lymph node. At the same time,
55 activated B and T cells and stromal cells (FRCs and lymphatic and blood endothelial cells) begin

56 proliferating[4,5]. During this initial phase, migratory DCs cause FRCs to relax and retract from, or
57 let go of, the collagen fibers, such that the collagen fibers bear most of the tension due to expansion
58 in size, and it is thought that the mesh spacing within the reticular network is increased[7-10]. As the
59 lymph node continues to expand, breaks occur in the collagen fibers and other extracellular matrix
60 (ECM) materials, requiring repair and transfer of some of the tension to the FRCs themselves[11].
61 Researchers have found permanent changes after the immune response is resolved and the tissue
62 is again at homeostasis because the outer capsule of the lymph node is thicker and stiffer[9].

63 Research has shown that the biomechanics, or tension and relaxation that also occur during
64 inflammation in the lymph nodes, can affect cell functions. The FRCs and collagen fibers are
65 hypothesized to provide a structural scaffold for B and T cells that regulates their proliferation and
66 migration, and also to distribute chemokines, cytokines, and growth factors throughout the lymph
67 node[12-15]. T cells respond to their environment by sensing and adapting to the biomechanics,
68 including fluid-like viscous and solid-like elastic stresses. Recently, researchers demonstrated that
69 T cells have higher expression of activation and inhibitory markers when exposed to slow relaxing,
70 more solid-like matrices, while T cells on fast relaxing, more fluid-like matrices had higher
71 expression of memory markers[16]. Biomechanics and viscoelasticity, the combined solid- and fluid-
72 like responses of a tissue, are largely dependent on ECM composition[19]. As we age, we accumulate
73 ECM materials in the lymph nodes (also known as fibrosis), and research has shown that the
74 motility of naïve T cells (circulating T cells prior to exposure to inflammatory stimuli) is decreased
75 in aged compared to young lymph nodes[17]. This is particularly evident near highly ECM-rich
76 fibrotic regions, which are likely to have increased solid-like elastic properties[17]. Aging also
77 appears to modulate naïve T cell numbers, which suggests that fibrosis and biomechanical
78 properties of the lymph nodes could be a contributing factor to age-related changes in our adaptive

immune response [18]. Interestingly, ECM composition and biomechanics of tissues is sex-dimorphic in many organs[20-22], and these differences may be a contributing factor to sex differences in susceptibility and progression of numerous diseases[20,23].

Despite the importance of ECM and viscoelasticity in the context of lymphocyte immunity, lymph node biomechanics and viscoelasticity have yet to be examined extensively, including in the context of inflammation. This is in part due to limitations to the methods available to study viscoelastic properties, traditionally via rheology[24] or atomic force microscopy[25,26]. A rheometer applies a shear or linear stress with a known displacement or speed on the sample and the resulting torque (or stress) the material responds with is recorded. While this is a satisfactory method for homogeneous substances, it is inadequate for samples like the lymph node since the spatial organization vital to its various functions is lost. Additionally, the rheometer usually requires a larger volume than what is available from smaller organs like the lymph nodes. Atomic force microscopy uses a cantilever that touches a sample surface at a constant force. The surface topography causes deflections in the cantilever, which alters the amount of laser light reflected from its surface and captured by a photodetector[25,26]. This readout can be used to infer the sample's viscoelastic response. While this method preserves the spatial organization of tissues, the analysis is limited to the sample surface and is sacrificial, making it less than ideal for studies aiming to look at both structure and function. Researchers have also used more specific methods, including tension nanoprobes to study lymph node elasticity[27], tensiometers to study capsule rigidity[28], 2-photon microscopy to study lymph node fibrosis[17], and nanoindentors to test lymph node viscoelasticity[9,29]. These methods have been helpful in elucidating lymph node biomechanics, but none of these are non-sacrificial nor provide biomechanical properties beyond the surface.

Using a previously published methodology[30,31], we combine nanoparticle-based multiple

102 particle tracking (MPT) microrheology with live lymph node slice culture, which allows us to
103 preserve tissue architecture ex vivo[32] while simultaneously studying lymph node viscoelasticity[30].
104 MPT uses nanoparticles of sizes close to, but smaller than, the mesh spacing of hydrogel-like
105 tissues and tracks their Brownian diffusive motion within the tissue over time[69-71]. The resulting
106 mean-squared displacement for each particle and the ensemble of all particles is then used to
107 determine biomechanical properties such as elastic and loss moduli, pore size, and microviscosity
108 of the lymph nodes[30,33-36]. Here, we investigate how the biomechanics of the lymph node change
109 during inflammation, particularly in the cortex and paracortex (B and T cell zones). We correlate
110 our microrheology measurements to structural changes in lymph node ECM and assess differences
111 in biomechanical responses to inflammation based on sex. Our study presents, for the first time,
112 an in-depth analysis of the complex biomechanics of distinct lymph node regions during an
113 inflammatory response in the context of tissue remodeling and sex, and lays the foundation for
114 future structure-function relationships between tissue biomechanics and lymphocyte functions.

115 **RESULTS**

116 **LPS induces peak inflammation in lymph nodes at day 3 and returns to homeostasis by day**
117 **14**

118 We inflamed the lymph nodes via intradermal injections of 10 μg lipopolysaccharide (LPS) in
119 female mice to simulate a bacterial challenge. After a single LPS challenge, lymph node mass
120 peaked on day 3 to nearly two-fold compared to untreated mice, started to decrease by day 5
121 ($p<0.1$), and returned to masses similar to untreated by day 7 (**Fig. 1A**). We quantified cell numbers
122 in the lymph nodes using flow cytometry (**Supp. Fig. S1C**) and found they first decreased from
123 4 ± 1 million in untreated to 1.8 ± 0.2 million in day 1 lymph nodes, followed by a significant
124 increase to 4.7 ± 0.7 million on day 3 (**Fig. 1B**). B cells significantly contributed to this increase

125 (**Fig. 1C**), as they increased in number from 0.9 ± 0.2 million cells in untreated to 2.2 ± 0.5 million
126 cells in day 3 lymph nodes (**Fig. 1C**). B cell numbers returned close to values for untreated mice
127 by day 7. While not significantly different, we observed that CD8+ and CD4+ T cell numbers also
128 appeared to contract at day 1 and expand again on day 3 (**Fig. 1D-F**).

129 **Peak inflammation increases biomechanical properties of the lymph nodes while reducing**
130 **pore size**

131 We used multiple particle tracking (MPT) to assess lymph node biomechanical properties,
132 including elastic and loss moduli, pore size, and microviscosity. After performing MPT, the
133 nanoparticles' mean squared displacement that occurs due to their Brownian motion in the lymph
134 node tissues can be used to extrapolate these various properties, and tissues typically exhibit both
135 elastic and viscous properties. The elastic modulus describes the solid-like properties of a material
136 and refers to how well it returns to its original shape after a force is applied (**Fig. 2A**). The loss
137 modulus describes the liquid-like properties of a material, or the viscous response, that
138 permanently deforms the sample (**Fig. 2A**). We used collagen III and B220 staining to delineate B
139 and T cell zones in the lymph nodes (**Fig. 2B**). We found that 500 nm nanoparticles freely diffuse
140 through the lymph node microenvironment, suggesting that this is the optimal size to probe the
141 'mesh' components, including cells and ECM, as well as fluid components, including interstitial
142 fluid (**Supp. Fig. S1A-B**). We observed a significant increase in lymph node microviscosity during
143 early stages of inflammation, with the overall viscosity reaching a peak value of 3.5 ± 1.2 Pa*s on
144 day 3 (**Fig. 2C)**. Lymph nodes had a significantly higher elastic modulus of 2.2 ± 0.7 Pa on day 3,
145 indicating a stiffer lymph node, compared to all other days (**Fig. 2D, 2E**). Lymph nodes begin to
146 return to elastic modulus values close to healthy by day 7 (0.2 ± 0.06 Pa) (**Fig. 2D-E**). We also
147 observed a significant increase in loss modulus on day 3, 1.9 ± 0.6 Pa, compared to untreated,

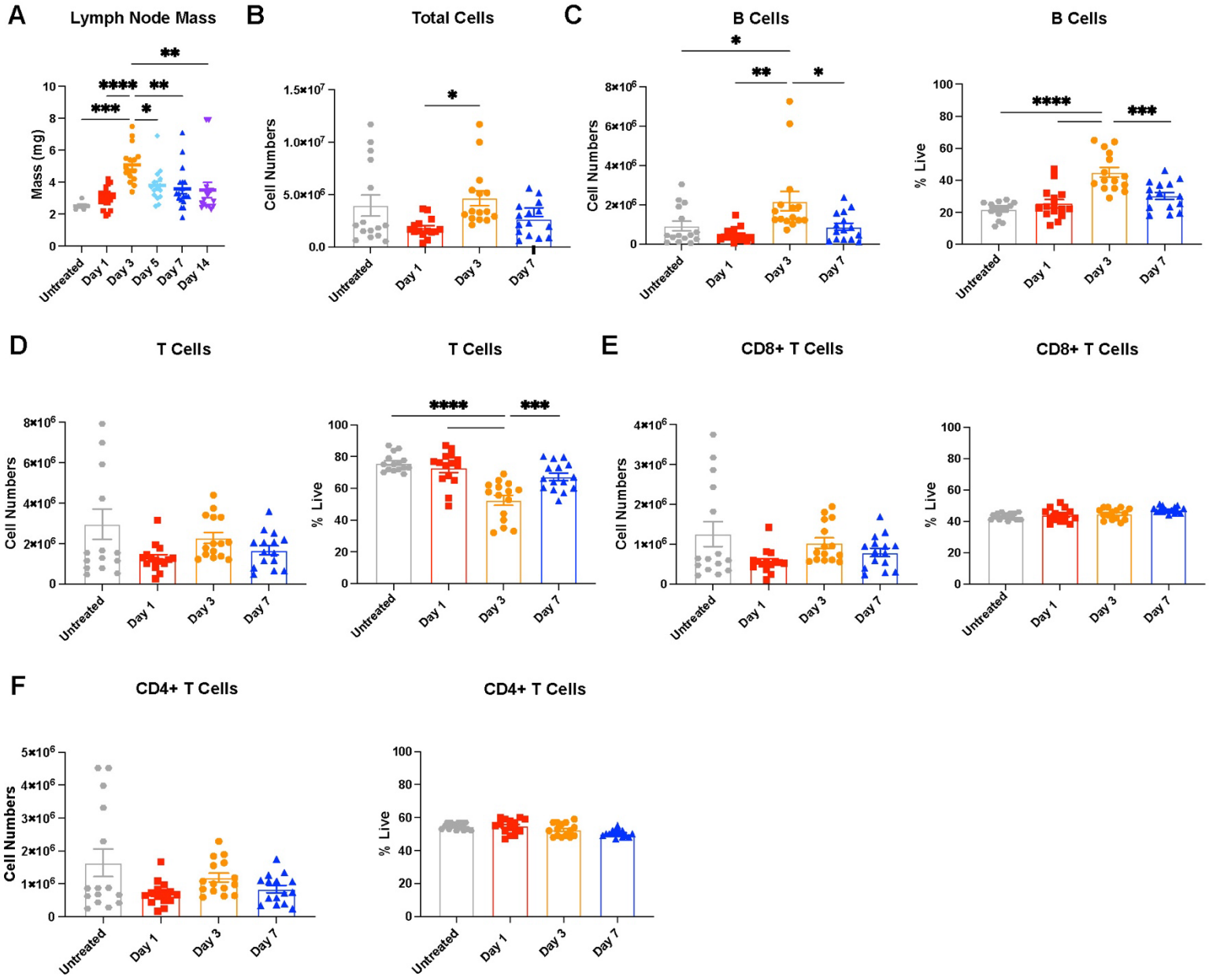

Figure 1. *Lymph nodes (LNs) expand and contract over 14 days post single stimulation with lipopolysaccharide (LPS)* (A) Mass of inguinal lymph node. (B) Total cell, (C) B cell (CD45+B220+), and (D) T cell (CD45+CD3+) numbers in lymph nodes collected by flow cytometry. (E) CD8+T cell (CD45+CD3+CD8+) and (F) CD4+ T cell (CD45+CD3+CD4+) numbers in lymph nodes collected by flow cytometry 1, 3, and 7 days post LPS stimulus. All values are reported as mean ± SEM. Statistical analysis performed by one-way ANOVA followed by Tukey's post-hoc test **(A-F)**. *p<0.05, **p<0.01, ***p<0.001, ****p<0.0001. N=10-15 female mice per group.

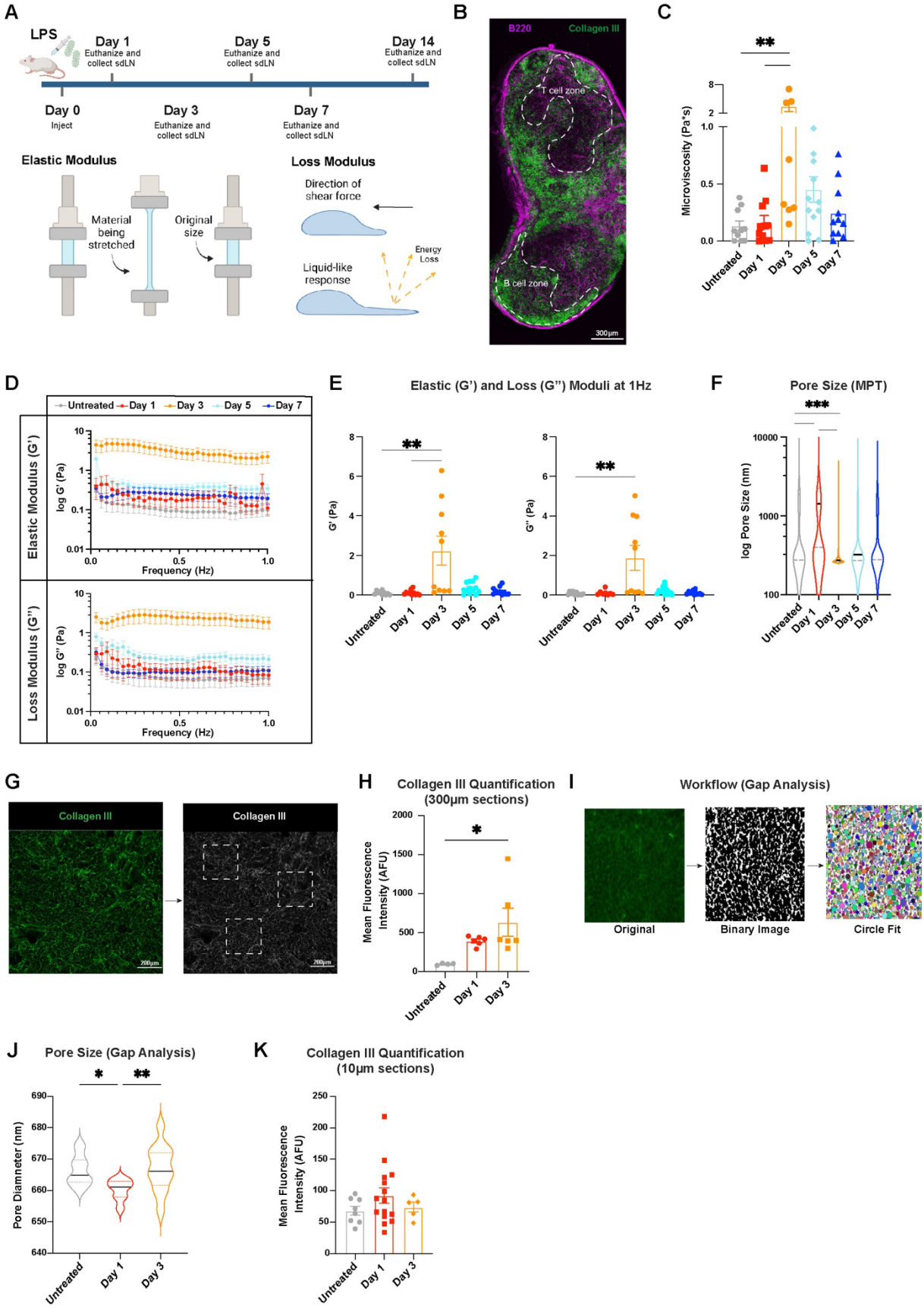

Figure 2 *Lymph node biomechanics change in response to LPS* (A) Injection schedule, schematic of elastic modulus, schematic of loss modulus (made with BioRender). (B) Lymph node slice stained for B220 (B cells) and Collagen III (ECM). (C) Microviscosity of the overall lymph node. (D) Elastic and loss moduli of overall lymph node over 1Hz and (E) at 1Hz. (F) Pore sizes (by MPT) in the overall lymph node. (G) Collagen III quantification workflow and (H) Collagen III quantification from confocal images using tissue slices (300µm thick) obtained using a vibratome. (I) Workflow of Gap analysis and (J) pore sizes measured by Gap analysis (PDPN staining). (K) Collagen III quantification using tissue slices obtained via cryosectioning (10µm thick). Median and quartile values shown for pore sizes. Other values are reported as mean ± SEM. Y-axis in **D, F** shown on a logarithmic scale, axes labeled with 'log' to enhance readability. Statistical analysis performed with 1-way ANOVA/Kruskal-Wallis tests followed by Tukey's/Dunn's multiple-comparisons post-hoc tests **(C,F,H,J,K)**. Elastic and loss moduli are compared at 1Hz as an average across all mice, and statistical analysis was done using Kruskal-Wallis test with Dunn's post-hoc analysis **(E)**. *p<0.05, **p<0.01, ***p<0.001, ****p<0.0001. N = 10-15 female mice.

148 0.07 ± 0.02 Pa, which indicates a high resistance to fluid flow at peak inflammation (**Fig. 2D-E**).
149 We found a significant increase in median pore size on day 1 of 1400 nm compared to 800 nm in
150 untreated lymph nodes, indicating tissue relaxation at the start of the inflammatory response (**Fig.**
151 **2F**). Pore size then decreased significantly to 270 nm on day 3 (**Fig. 2F**) and began to increase
152 again thereafter. Our data indicate that changes in lymph node elastic and loss moduli are closely
153 related to changes in cell proliferation during acute inflammation.

154 To understand underlying causes for changes in pore size, we semi-quantitatively assessed the key
155 ECM component in the lymph node, collagen III, via fluorescence microscopy (**Fig. 2G**). We used
156 either 10µm (obtained via cryostat) or 300µm (obtained via vibratome) thick lymph node sections.
157 In the thicker vibratome slices, we found a significant increase in collagen III mean fluorescent
158 intensity (MFI) from 98 ± 6 AFU in untreated to 640 ± 180 AFU on day 3 (**Fig. 2H**). This data
159 suggests that increases in collagen density may contribute to the decreased pore size observed on
160 day 3 (**Fig. 2F**). In addition, using thin, 10µm lymph node slices stained for podoplanin, a marker
161 of FRCs, in conjunction with a MATLAB script, Gap analysis[7], we calculated pore sizes within
162 the reticular network. Gap analysis fits circles of the largest possible diameter into binarized
163 images of stained tissue to identify and measure non-overlapping gap sizes (**Fig. 2I**). The pore
164 sizes obtained using this method showed different trends to those obtained from MPT data: the
165 median pore size reduced slightly from 670 nm in untreated to 660 nm on day 1 and increased
166 again on day 3 to 670 nm (**Fig 2J**). These trends were likely different since, unlike MPT, Gap
167 analysis does not take into consideration presence of the effects due to cells or other non-collagen
168 materials during the analysis of pore size. We also found no differences in collagen MFI in thin
169 sections (**Fig 2K**). These contrasts highlight that 'pore size' or 'mesh spacing' is not a uniform
170 metric; the characterization method used can substantially influence both the measured values and

171 their interpretation in hydrogel-like tissues.

172 **B and T cell zones exhibit similar biomechanical responses during acute inflammation**

173 B and T cell zones, or cortex and paracortex, in the lymph nodes serve unique functions that lead
174 to B and T cell activation during an inflammatory response. Given the distinct functional roles of
175 B and T cell zones, we next assessed whether their biomechanical properties differed. Surprisingly,
176 the microrheological profiles of the two compartments were similar. Mean microviscosity values
177 were comparable, ranging from 0.055 – 2.3 Pa*s in the B cell zone to 0.16 – 3.8 Pa*s in the T cell
178 zone (**Fig. 3A**), with both reaching a peak at day 3. Notably, despite these similarities, individual
179 measurements varied considerably between mice (**Supp. Fig. S2A**), highlighting substantial inter-
180 animal heterogeneity. Similarly, we found that trends in elastic and loss moduli were comparable
181 between both zones, with both reaching a maximum value at day 3 **(Fig 3B-C).** However, direct
182 comparisons at each time point (**Supp. Fig. S2B**) showed no significant differences between the
183 two compartments. These findings, together with the microviscosity data, indicate that B and T
184 cell zones exhibit similar biomechanical behavior during acute inflammation.

185 In both the B and T cell zones, there was an initial increase in pore size. In the B cell zone, median
186 pore size increased from 1300 nm in untreated to 1900 nm on day 1 and then decreased to 280 nm
187 on day 3, followed by an increase to 350 nm on day 5 and 1100 nm on day 7 (**Fig. 3D**). Similarly,
188 the T cell zone median pore size increased from 290 nm in untreated to 1700 nm on day 1 and then
189 decreased to 270 nm on day 3 and remained relatively stable at 320 nm on day 5 and 290 nm on
190 day 7, similar to the pore size of untreated lymph nodes (**Fig. 3D**).

191 **Lymph node biomechanics change permanently after resolution of acute inflammation**

192 Two weeks after inflammation is induced, the overall cell numbers in the lymph node have

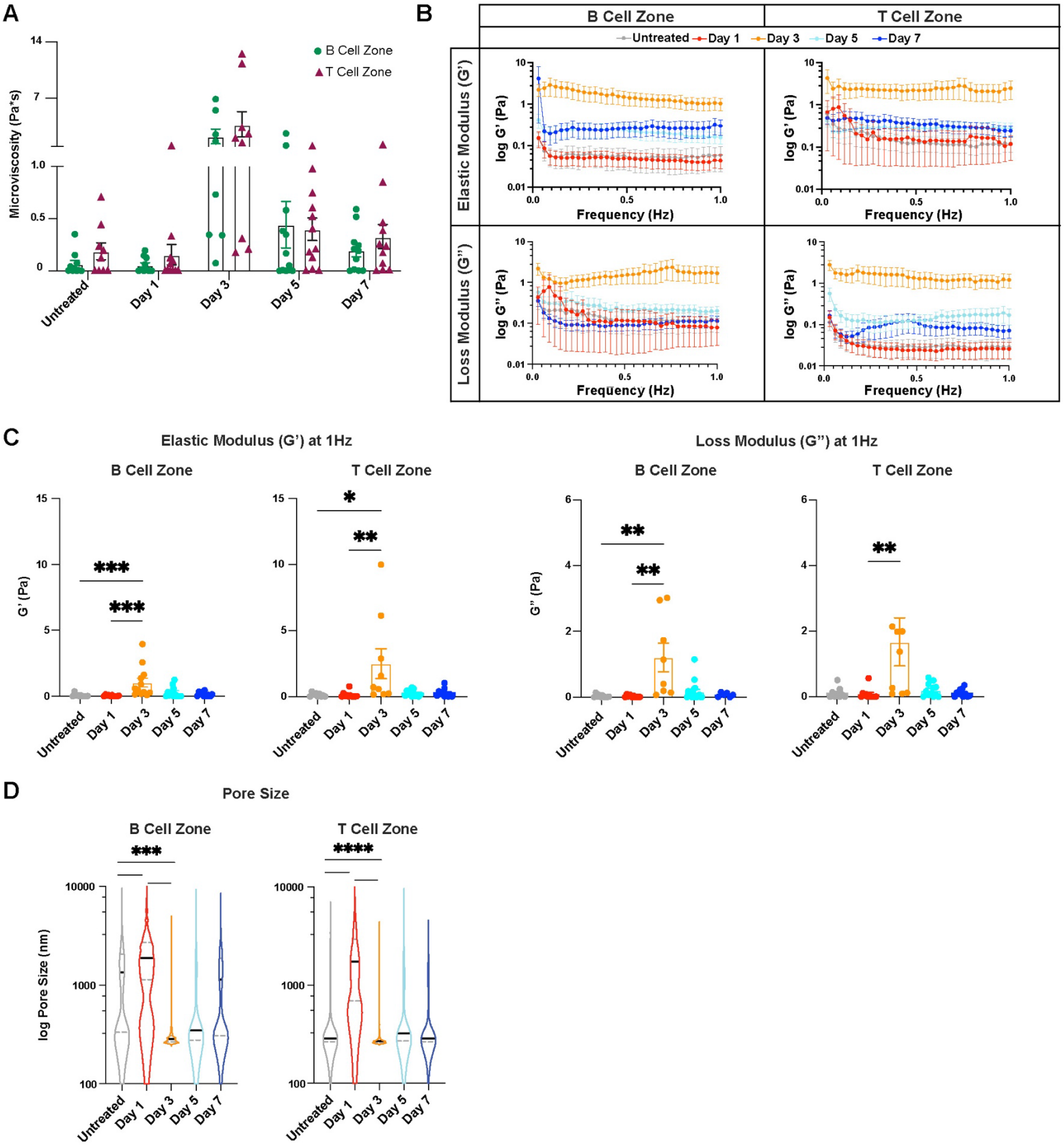

Figure 3 *B and T cell zone biomechanics change in a similar fashion during immune response to LPS* (A) Microviscosity of the B and T cell zones in untreated lymph nodes and lymph nodes days 1, 3, 5, and 7 after LPS treatment. (B) Elastic and loss moduli of B and T cell zones over 1Hz and (C) at 1Hz. (D) Pore sizes (by MPT) of B and T cell zones during the course of inflammation. Median and quartile values shown for pore sizes. Other values are reported as mean ± SEM. Y-axis in **B, D** shown on a logarithmic scale, axes labeled with 'log' to enhance readability. Statistical analysis of zone-wise comparison of microviscosity was performed using a Mann-Whitney test on each day **(A)**, elastic and loss moduli are compared at 1Hz as an average across all mice, and statistical analysis is was performed with a Kruskal-Wallis test with Dunn's post-hoc analysis **(C)**. Statistical analysis for pore size was done using a Kruskal-Wallis test followed by Dunn's post-hoc test **(D)**. *p<0.05, **p<0.01, ***p<0.001, ****p<0.0001. N = 10-15 female mice.

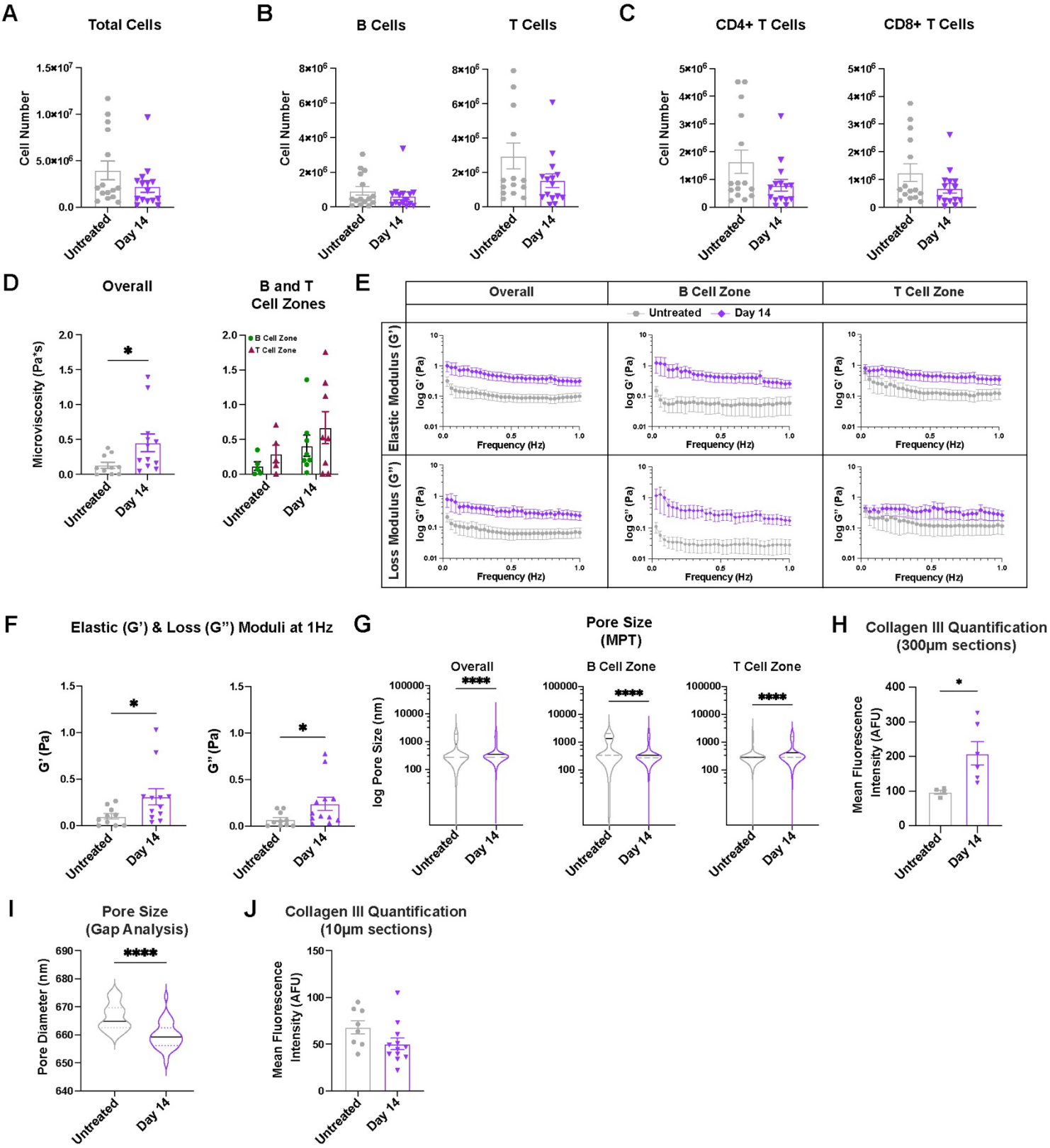

Figure 4 *Lymph node biomechanics show permanent changes at resolution, two weeks after acute inflammatory challenge with LPS* (A) Total cell, (B) B cell (CD45+B220+),T cell (CD45+CD3+), and (C) CD8+ T cell (CD45+CD3+CD8+) and CD4+ T cell (CD45+CD3+CD4+) numbers in lymph nodes from untreated mice and mice 14 days post LPS stimulation analyzed by flow cytometry. (D) Microviscosity in the overall lymph node and in the B and T cell zones from untreated mice and mice 14 days post LPS stimulation. Elastic and loss moduli over (E) 1 Hz and (F) at 1 Hz in the overall lymph node and in the B and T cell zones from untreated mice and mice 14 days post LPS stimulation. (G) Pore sizes (by MPT) in the overall lymph node and in the B and T cell zones. (H) Collagen III quantification from confocal images using tissue slices obtained via vibratome (300µm thick) (I) Pore sizes measured by Gap analysis (PDPN staining). (J) Collagen III quantification using tissue slices obtained from a cryostat (10µm thick). Median and quartile values shown in pore sizes. Other values are reported as mean ± SEM. Y-axis in **E, G** shown on a logarithmic scale, axes labeled with 'log' to enhance readability. Statistical analysis performed by a t-test/Mann-Whitney test **(A-D, G, H, I)**. Statistical analysis of zone-wise comparison of microviscosity was performed with a Mann-Whitney test at each timepoint **(D)**. Elastic and loss moduli are compared at 1Hz as an average across all mice, and statistical analysis is done via Mann-Whitney test **(E,F)**. *p<0.05, **p<0.01, ***p<0.001, ****p<0.0001 N = 10-15 female mice.

193 contracted to 2 ± 0.6 million cells, similar to levels in untreated lymph nodes (4 ± 1 million cells,
194 (**Fig. 4A**). Similarly, B cell and T cell numbers (**Fig. 4B**), including CD4+ and CD8+ T cell subsets
195 (**Fig. 4C**), return to levels similar to untreated. These data suggest that at day 14, lymph node cell
196 composition has returned to states similar to untreated, and resolution has occurred. However, we
197 have also found that biomechanical properties of the lymph nodes do not fully return to baseline.
198 Lymph node microviscosity increased 3.5-fold on day 14 compared to untreated (**Fig. 4D**). Though
199 not significantly different, B cell zone microviscosity appeared to be lower than T cell zone
200 microviscosity for both untreated and day 14 (**Fig. 4D**). We found a higher elastic modulus, 0.3 ±
201 0.09 Pa, and loss modulus, 0.2 ± 0.07 Pa, on day 14 compared to 0.1 ± 0.03 Pa and 0.07 ± 0.02 Pa
202 for untreated, respectively, (**Fig. 4E-F**), indicating an overall stiffer tissue that had higher
203 resistance to flow. These data suggest that lymph nodes on day 14 are permanently restructured
204 after a single immune challenge. B cell zones appeared to drive much of these changes, as a greater
205 increase on day 14 was observed for both loss and elastic moduli compared to T cell zones (**Fig.**
206 **4E**). We also found a significant decrease in median pore size on day 14 (350 nm) compared to
207 untreated (800 nm) (**Fig. 4G**). Additionally, we found an increase in collagen III on day 14 in thick
208 sections compared to untreated **(Fig. 4H).** When assessing pore size based on staining only for the
209 FRC network (podoplanin) using Gap analysis, we also found a slight reduction in pore size at day
210 14 compared to untreated, and thin sections revealed no differences in collagen III **(Fig. 4I-J).**
211 Differences in the values of pore size and collagen quantifications for these two methods are likely
212 due to considering a larger (300 μm MPT/thick sections) or smaller (10 μm Gap
213 analysis/cryosections) section of the lymph nodes.

214 **Changes in lymph node biomechanics during inflammation are sexually dimorphic**

215 To determine whether biological sex influences lymph node biomechanics during an acute
216 inflammatory response, we compared the biophysical properties of the lymph nodes between male
217 and female mice at days 3 and 14 post injection, in addition to untreated, to assess differences at
218 peak inflammation and resolution, respectively. We found that female lymph nodes exhibit slightly
219 higher elastic moduli already in untreated states, with 0.11 ± 0.03 Pa in female mice and 0.05 ±
220 0.004 Pa in male mice (**Fig. 5A-B**), though not significant. At day 3, lymph nodes had significantly
221 higher elastic moduli in female compared to male mice, with 2.2 ± 0.7 Pa vs. 0.01 ± 0.003 Pa,
222 respectively. On day 14, lymph nodes from female mice continued to exhibit higher elastic moduli
223 than those from male mice with 0.3 ± 0.08 Pa vs. 0.05 ± 0.01 Pa (**Fig. 5A-B**), respectively. We
224 found similar results for loss moduli, where the moduli in lymph nodes from female mice were
225 higher compared to those from male mice for both day 3, with 1.9 ± 0.6 Pa (female) vs. 0.005 ±
226 0.001 Pa (male), and day 14, with 0.23 ± 0.07 Pa (female) vs. 0.02 ± 0.006 Pa (male) (**Fig. 5A-B**).
227 We also found that while elastic moduli and loss moduli reach a peak at day 3 in female mice, they
228 reach a minimum in male mice (**Fig. 5A**). Additionally, we found lower median pore sizes (270
229 nm vs 1600 nm) (**Fig. 5C**) and higher mean viscosity (3.5 ± 1.1 Pa*s vs. 0.009 ± 0.002 Pa*s) (**Fig.
230 5D**) on day 3 in lymph nodes from female vs. male mice. Similar trends were observed within the
231 B and T cell zones in lymph nodes of male and female mice at all time points (**Supp. Fig. S3A-C,
232 S4A-B).** Additionally, like female mice, there were no biomechanical differences observed
233 between the B and T cell zones in male mice. When assessing lymph node biomechanics at
234 resolution of inflammation, we found a return to baseline values for both elastic moduli (0.05 ±
235 0.01 Pa vs. 0.05 ± 0.01 Pa) and loss moduli (0.02 ± 0.005 Pa vs. 0.02 ± 0.006 Pa) in male mice
236 **(Fig 5E)**. However, for female mice, both elastic (0.3 ± 0.08 Pa at day 14 vs. 0.1 ± 0.03 Pa in

237 untreated) and loss moduli (0.23 ± 0.07 Pa at day 14 vs. 0.07 ± 0.02 Pa in untreated) were increased
238 at day 14 (**Fig. 5E**). Independent B and T cell zone restructuring was observed only in lymph nodes
239 from female (**Fig. 4E-F)** mice (**Supp. Fig. S4C).** These data suggest that biological sex influences
240 lymph node restructuring during and after resolution of acute inflammation.

241 **Chronic inflammation does not modulate lymph node biomechanics**

242 Given our findings that acute inflammation induces changes in lymph node biomechanics, we next
243 sought to understand if these changes are enhanced during chronic inflammation. To induce
244 chronic inflammation, 10 μg LPS was intradermally injected weekly for 5 weeks and mice
245 euthanized days 3 and 14 after the final injection were chosen to assess lymph node biomechanics
246 (**Fig. 6A**). Chronically inflamed lymph nodes trended toward more cells on days 3 and 14 (3 ± 0.8
247 million cells and 2 ± 0.7 million cells, respectively), compared to untreated (0.5 ± 0.09 million
248 cells) (**Fig. 6B**). Compared to untreated (0.1 ± 0.01 million), B cell numbers were increased on
249 day 3 (1 ± 0.4 million) and day 14 (0.6 ± 0.2 million) (**Fig. 6C**). Similarly, there was a trend toward
250 total T cell numbers on day 3 (1.6 ± 0.3 million) and day 14 (1.2 ± 0.4 million) compared to
251 untreated (0.4 ± 0.1 million) (**Fig. 6C**). CD4+ and CD8+ T cell numbers also trended higher on
252 day 3 (0.9 ± 0.2 million and 0.6 ± 0.01 million, respectively) compared to day 14 (0.7 ± 0.2 million
253 and 0.4 ± 0.2 million) (**Fig. 6D**). While the total numbers of total cells, B cells, and T cells were
254 only trending toward significant (p values for all were $p<0.15$), the percent live of each of these
255 was significantly higher at day 3 compared to untreated. By day 14 after the final injection, all cell
256 numbers decreased again and were not significantly different to untreated.

257 Biomechanical properties of chronically inflamed lymph nodes appeared to be similar 3 days and
258 14 days after final injection and remained similar to untreated. Chronically inflamed lymph nodes
259 had microviscosities of 0.1 ± 0.04 Pa*s for untreated, 0.1 ± 0.06 on day 3, and 0.3 ± 0.1 Pa*s on

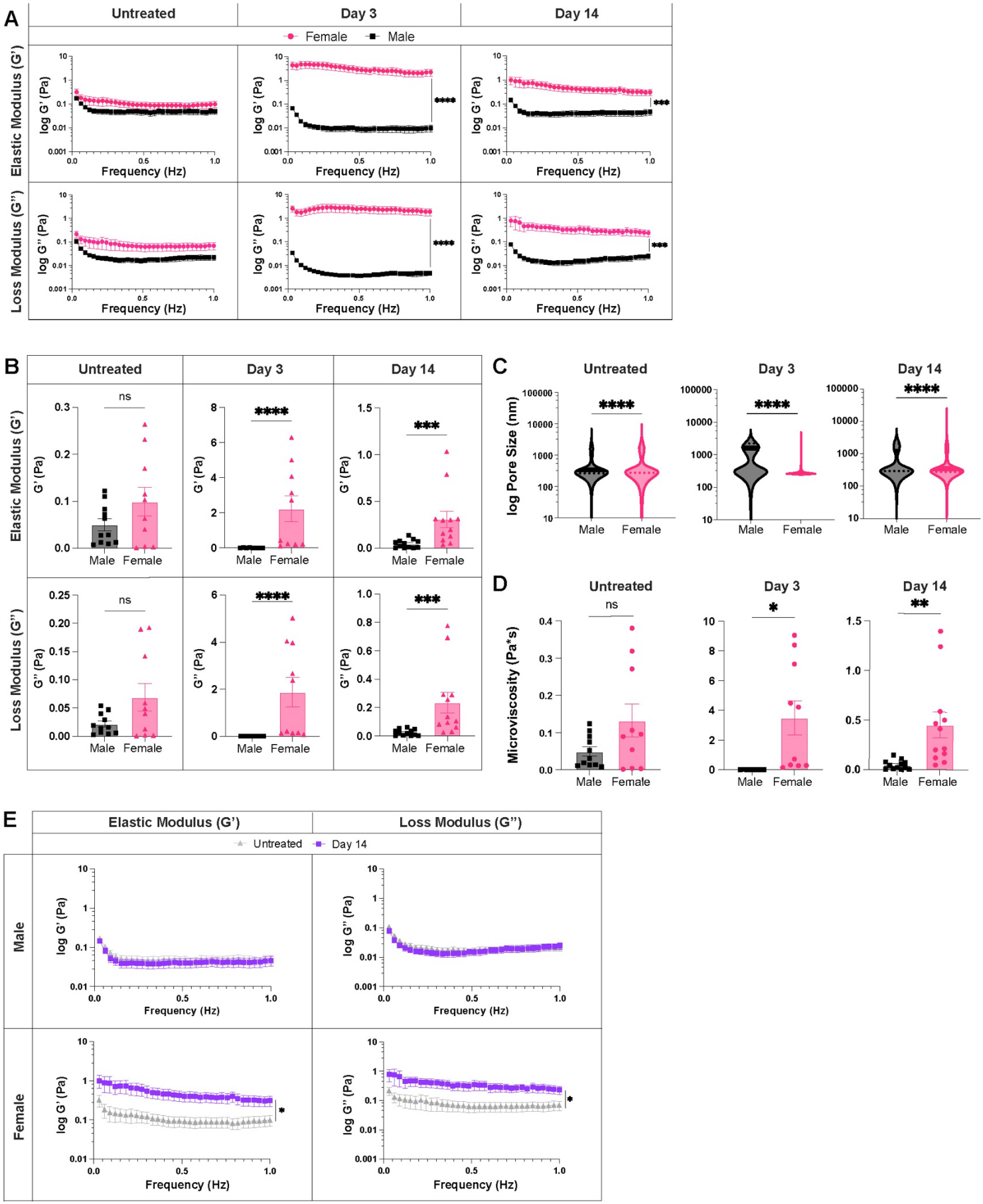

Figure 5 *Lymph node biophysical properties are sexually dimorphic* Elastic and loss moduli for male and female lymph nodes (A) over 1Hz and (B) at 1Hz. (C) Overall pore size (by MPT), and (D) microviscosity of healthy and acutely inflamed male and female lymph nodes. (E) Elastic and loss moduli of male and female lymph nodes for untreated and day 14 lymph nodes over 1Hz. Median and quartile values shown in pore sizes. Other values are mean ± SEM. Y-axis in **A, C, E** shown on a logarithmic scale, axis labelled with 'log' to enhance readability. Statistical analysis by Mann-Whitney test (**B,C**) or Welch's t-test (**D**). Elastic and loss moduli are compared at 1Hz as an average across all mice, and statistical analysis is done by t-test/Wilcoxon rank-sum test(**A,B,E**). Significance values are denoted on **A,E** for representation.*$p<0.05$, **$p<0.01$, ***$p<0.001$, ****$p<0.0001$, ns $p\geq0.05$. N=8-12 male or female mice.

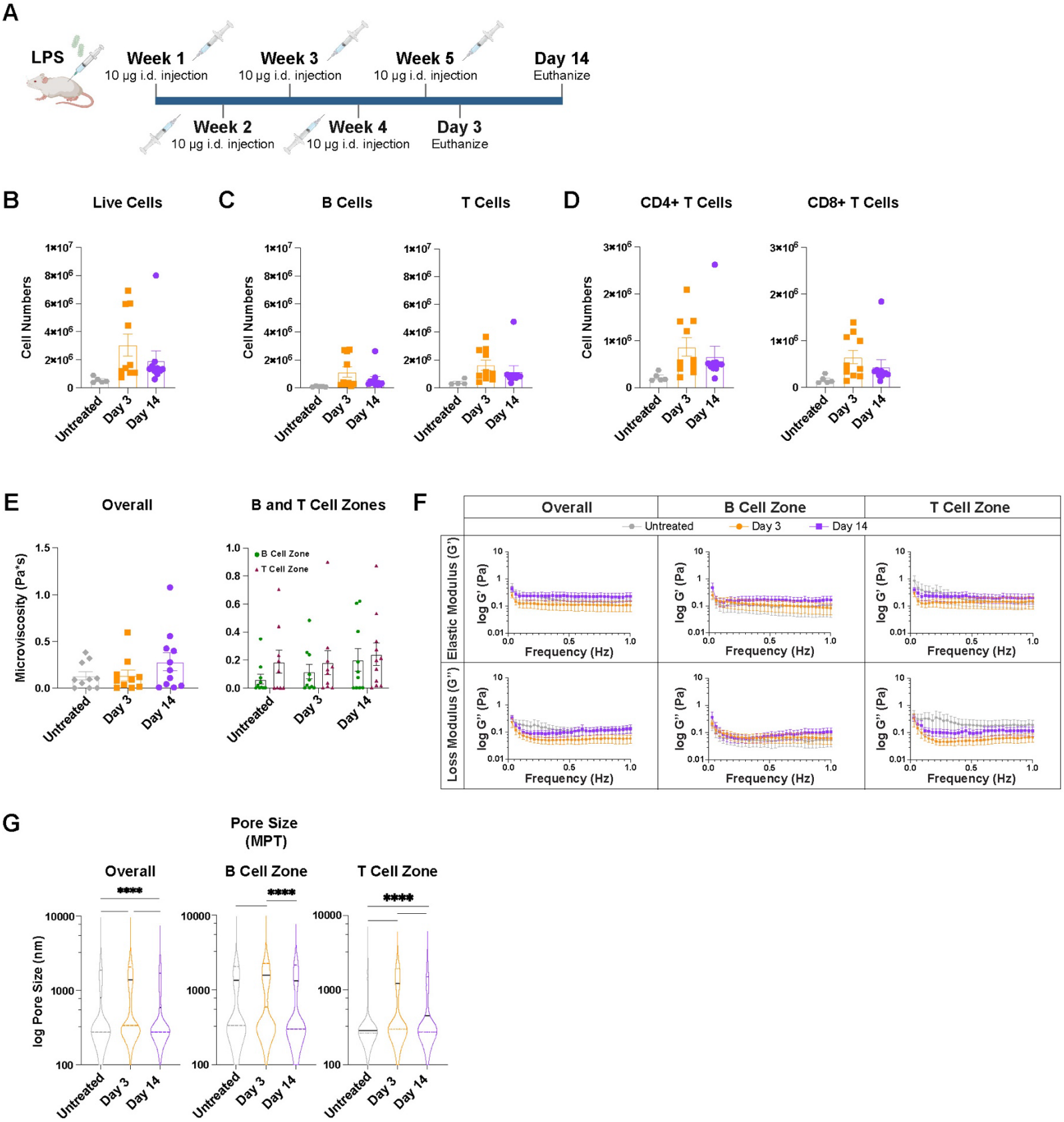

Figure 6 *Chronic inflammation does not modulate lymph node biomechanics* (A) Injection timeline for chronic inflammation studies (B)Total cell, (C) B cell ($CD45^+B220^+$) and T cell ($CD45^+CD3^+$), and (D) CD8+ T cell ($CD45^+CD3^+CD8^+$) and CD4+ T cell ($CD45^+CD3^+CD4^+$) numbers from untreated and chronically inflamed lymph nodes analyzed by flow cytometry. (E) Microviscosity (F) elastic and loss modulus over 1 Hz, and (G) pore sizes (by MPT) in the overall lymph node and in the B and T cell zones of untreated chronically inflamed lymph nodes. Median and quartile values shown in pore sizes. Other values are reported as mean ± SEM. Y-axis in **F,G** shown on a logarithmic scale, axis labelled with 'log' to enhance readability. Statistical analysis by 1-way ANOVA/Kruskal-Wallis test followed by Tukey's/Dunn's multiple-comparisons post-hoc test **(B-D, E, G)**. Statistical analysis of zone-wise comparison of microviscosity was done by a Mann-Whitney test on each day **(E)**. Elastic and loss moduli are compared at 1Hz as an average across all mice, and statistical analysis is done by Kruskal-Wallis Test **(F)**. *p<0.05, **p<0.01, ***p<0.001, ****p<0.0001. N = 10-15 female mice.

260 day 14 (**Fig. 6E**). T and B cell zones also had similar microviscosities on day 3 (0.2 ± 0.08 and 0.1
261 ± 0.05 Pa*s, respectively) and day 14 (both 0.2 ± 0.08 Pa*s) (**Fig. 6E**). Elastic moduli in lymph
262 nodes were also similar on day 3 (0.1 ± 0.05 Pa*s), day 14 (0.2 ± 0.08 Pa*s), and for untreated
263 (0.09 ± 0.03 Pa) (**Fig. 6F**). Elastic moduli were slightly lower on day 3 compared to day 14 in both
264 B (0.08 ± 0.04 Pa and 0.2 ± 0.06 Pa, day 3 and 14, respectively) and T cell zones (0.15 ± 0.07 Pa
265 and 0.2 ± 0.08 Pa, day 3 and 14, respectively) (**Fig. 6F**), though this was not significant. Loss
266 moduli were similar on day 3 (0.06 ± 0.02 Pa*s) and day 14 (0.1 ± 0.05 Pa*s) compared to
267 untreated (0.07 ± 0.02 Pa) (**Fig. 6F**). Loss moduli were also similar at days 3 and 14 in B (0.06 ±
268 0.03 Pa and 0.1 ± 0.04 Pa, day 3 and 14, respectively) and T cell zones (0.07 ± 0.02 Pa and 0.1 ±
269 0.04 Pa, day 3 and 14, respectively) (**Fig. 6F**). Median pore size within the lymph node
270 significantly increased from 800 nm in untreated to 1400 nm on day 3 (**Fig. 6G)**; this was true for
271 both B (1300 nm in untreated to 1600 nm at day 3) and T (300 nm in untreated to 1200 nm at day
272 3) cell zones (**Fig. 6G)**. These patterns remained true one month ("long-term resolution") after the
273 final LPS challenge. Median pore sizes within the lymph node were significantly increased from
274 untreated (800 nm) to long-term resolution (1200 nm) (**Supp. Fig. S5A**), as well as in the B (1300
275 nm untreated to 1400 nm long-term) and T (300 nm untreated to 1100 nm long-term) cell zones
276 (**Supp. Fig. S5A**). Elastic and loss moduli remained similar to untreated at long-term resolution
277 both overall and in the B and T cell zones **(Supp. Fig. S5C)**.

278 **DISCUSSION**

279 Elucidating the role of the influence of biomechanical stimuli on immune cell behavior and
280 function has been an area of active interest[37-39]. In this study, we examined the biomechanical
281 properties of the lymph node, a central pillar involved in the coordination of immune response.
282 Using multiple particle tracking (MPT) microrheology[30,31,36], a minimally invasive technique, we

283 provide a comprehensive analysis of lymph node biomechanics (elastic/loss moduli, pore size,
284 microviscosity) during homeostasis and over the course of acute and chronic inflammation,
285 including at resolution. We found that biomechanics of B and T cell zones change in a similar
286 fashion during acute inflammation, and that changes in biomechanical properties are sex
287 dependent. Our work suggests that restructuring may in part depend on changes in extracellular
288 matrix (ECM) composition, and that chronic inflammation does not cause the same differences in
289 biomechanical response as acute inflammation.

290 Lipopolysaccharide (LPS) initiates a TLR-4 response, which resulted in a lymph node expansion-
291 contraction cycle that lasted approximately 14 days. Lymph nodes increase in size as soon as 1 day
292 post initial stimulus and reach an inflammation peak at day 3 after LPS stimulation. We observed
293 that an initial increase in the pore size at day 1 compared to untreated counterparts matches prior
294 observations that the inter-network spacing of the reticular network is increased during the initial
295 phases of lymph node expansion[7,8,10,11,40]. However, we did not detect a reduction in elastic and
296 loss moduli at day 1, unlike previous reports[6,8,10] that describe a 'priming phase', in which network
297 tension decreases, or 'relaxes', during early phases of lymph node expansion. This 'relaxation'
298 reflects a shift in load bearing from the conduits to cells in the fibroblastic reticular cell (FRC)
299 network, features which our microrheological approach may not be able to directly resolve. In
300 addition, immune response kinetics to LPS alone may likely differ from those of antigen-adjuvant
301 models used prior, with earlier stages dominated by innate activation, leading to the altered
302 mechanical trajectories we observed. By peak inflammation (3 days post injection), lymph nodes
303 are nearly doubled in size, on account of increased cellularity. Previous studies[4,5,7,9] have shown
304 that lymphocyte influx plays a key role in lymph node swelling mechanics and that perturbing the
305 entry of lymphocytes leads to both a lowered viscosity and lymph node volume[9]. Lymph node

306 swelling is also associated with stretching of the reticular network and changes to FRC size[8,9,40].
307 We note the increased cellularity at day 3 corresponds to a decrease in pore size and the higher
308 viscosity echoes trends reported earlier. A consequence of increased cellularity could be a decrease
309 in interstitial fluid density within the lymph node, which coupled with reduced pore sizes, may
310 result in altered cell migration patterns within the lymph node. Smaller pores reduce the ease of
311 nuclear movement for migrating cells[42], which can have adverse effects on their survival[43,44] as
312 they navigate through the complex lymph node microenvironment. Interestingly, we observed a
313 high degree of heterogeneity in the rheological data obtained at day 3, likely reflecting both
314 biological and structural variability at peak inflammation. Differences in cell packing due to
315 increased cellularity, variations in FRC network tension, and individual response trajectories
316 across mice[8] may contribute to the observed rheological differences, despite synchronized
317 sampling. Further, active cellular processes such as cell migration, enzymatic remodeling, or
318 fibrosis can also cause microscale changes in the tissue structure. These changes are spatially and
319 temporally heterogeneous during immune response and can lead to additional variations in the
320 measured microviscosity and moduli. Consequently, while MPT is a powerful tool, future
321 investigations integrating it with other high-throughput biophysical techniques or imaging
322 approaches will help provide a more comprehensive understanding of complex tissue
323 biomechanics.

324 Quantifying the morphology—particularly the pore size or mesh spacing—of hydrogels
325 and hydrogel-like tissues has been a long-standing interest in tissue engineering, drug delivery,
326 and the study of cell migration[62-66]. The pore size distribution significantly impacts the mechanical
327 properties, such as elastic and loss moduli, of hydrogels and tissues. Therefore, precise
328 determination of pore sizes has broad implications for a wide range of biomedical applications.

329 The term ‘pore size’ is often used as a blanket descriptor, yet its definition and interpretation rely
330 heavily on the measurement method. In our study, we used two approaches, Gap analysis and MPT,
331 to estimate the pore size of lymph node tissue. Gap analysis provides a direct, spatial estimate of
332 pore size, measuring the physical space between elements of the podoplanin-stained reticular
333 network. In contrast, MPT yields an indirect, dynamic, and temporally informed metric based on
334 individual particle movement within the complete tissue instead of a single stained component.
335 This allows it to integrate the influence of cells, ECM, and all tissue components, not just the FRC
336 network, on pore size. Each method has its own limitations: Gap analysis is restricted by a limited
337 field of view and is susceptible to artifacts introduced during sample processing and image
338 stitching. MPT, as a 2D approximation, cannot resolve errors due to 3D particle motion, and is
339 sensitive to noise that may skew particle mobility measurements. The differences in our results
340 highlight that studies of pore size in complex tissues, such as the lymph node, are not always
341 directly comparable, and the characterization method should therefore be explicitly considered
342 when interpreting or generalizing ‘mesh spacing’ in tissues. We also observed a negative
343 correlation between pore size and collagen III deposition, suggesting increased ECM deposition
344 may be responsible for changes in tissue morphology, and consequently tissue biomechanics.
345 Exploring the relative contributions of the ECM on lymph node biomechanics is a key area for
346 subsequent investigation.

347 Our work also revealed that the B and T cell zones of the lymph node exhibit similar
348 restructuring patterns. The microviscosity and elastic and loss moduli exhibit no differences across
349 the zones during acute inflammation. Interestingly, however, the B and T cell zones exhibit
350 different trends in pore size, and the ratio of B to T cell zone pore sizes shows an increasing trend
351 over the course of an immune challenge, suggesting a higher degree of reorganization in the B cell

352 zones. These data reflect similar patterns observed in other studies that highlight changes in the
353 relative volume fractions of the B cell zone and T cell zone in the lymph node following antigen
354 stimulation - there was a notable increase in the size of the B cell zone with a concurrent decrease
355 in the T cell zone. Differences in restructuring may be due to the maturation of follicles to germinal
356 centers at different time points. B cells undergo somatic hypermutation over time and these cellular
357 changes may affect restructuring. The prevailing view is that the overall changes in lymph node
358 structure were largely due to the reticular network in the T cell zone[9,13,15,45], but these findings
359 indicate that the B cell zone may play a larger role than previously thought.

360 The prevalence of sex bias in immune cell counts and immune response between males
361 and females is well documented[46-48]. Here, we demonstrated for the first time that biological sex
362 also influences the mechanical properties and restructuring of lymph node tissue during acute
363 inflammatory response. Lymph nodes in female mice exhibit higher elastic and loss moduli than
364 lymph nodes from male mice over the course of immune response. A higher elastic modulus
365 indicates tissues are more resistant to deformation (stiffer), whereas a higher loss modulus
366 indicates tissues dissipate more energy under deformation, indicating a higher degree of internal
367 friction. From a structural or biochemical perspective, higher elastic and loss moduli could reflect
368 alteration of ECM structure in a sex-specific fashion due to differences in matrix protein
369 concentrations, alignment, or densities[72]. Interestingly, 3 days post inflammatory stimulus, we
370 observe a peak in elastic/loss moduli in female lymph nodes but a minima in male lymph nodes.
371 This reversal of trends could be indicative of males and females exhibiting differing immune
372 response rates to LPS, which may be influenced by sex hormones. Indeed, several clinical studies
373 and in vitro models have demonstrated higher proinflammatory cytokine release[49-52] in males
374 compared to females. Conversely, there is evidence to suggest that the influence of male sex

375 hormones, androgens, may have an inhibitory effect[53,54], leading to sex-based discrepancies and a
376 diminished immune response in males. One study suggests that the TLR4 receptor, responsible for
377 detection of LPS, may be regulated by testosterone. They found TLR4 expression on macrophages
378 was reduced in the presence of testosterone in vitro, and surgical castration led to an increase in
379 TLR4 expression and elevated inflammatory response in male mice[55]. Another study[56]
380 demonstrated that androgens down regulated the number of skin-resident dendritic cells and
381 lowered their migratory capacity to lymph nodes in male mice. While the effect of androgens may
382 provide an explanation for our observations during lymph node expansion, additional research is
383 needed to accurately assess the effect of sex hormones on lymph node biomechanics during the
384 resolution phase of acute inflammation.

385 Disease states such as chronic inflammation, and even aging, have been shown to alter
386 lymph node structure as well as impair immune function[17,57]. In aging, there is an increase in
387 collagen deposition and a blurring of boundaries between B and T cell zones in the lymph
388 nodes[18,58,59]. This suggests that aging may result in stiffer lymph node tissue environments, and
389 research has shown that viscoelasticity can modulate T cell functions, including expression of
390 activation vs. memory markers[16]. Furthermore, aging appears to reduce T cell migration speed and
391 linearity, which is also exacerbated in regions close to the extracellular matrix, suggesting that the
392 biophysical environment surrounding T cells can affect their functions[17]. One hypothesis in aging
393 is that the repeated inflammatory insults we experience throughout our lives cause permanent
394 lymph node remodeling. We sought to mimic this by inducing chronic inflammation, but our data
395 suggest that at least after one month of inflammation, there are minimal biophysical changes in the
396 lymph nodes. However, our study may be limited by the length and type of inflammatory cues we
397 used [67,68]. Remodeling of tissues in chronic inflammation may be slower than the time scales we

398 observed; thus, future research investigating how different types of inflammation and duration of
399 chronic inflammatory stimuli impact lymph node biophysical properties would provide valuable
400 insights and enhance the generalizability of our findings.

401 In summary, the role of biomechanics is heavily understudied in the context of immune
402 responses, particularly in the lymph nodes. This study investigated for the first time how the
403 biomechanics of the lymph node are altered during acute and one-month long inflammation, and
404 highlights the vital role of both the reticular network and lymph node architecture in modulating
405 lymph node biophysical properties over the course of an acute inflammatory response. It also sheds
406 light on the role of biological sex on lymph node biomechanics, providing an additional complexity
407 to known sex differences in immune responses. Our work provides new insights into structure-
408 function relationships in the lymph node and underscores the growing importance of tissue
409 mechanics in understanding immune response.

410 **MATERIALS AND METHODS**

411 **Animal work**

412 Female and male C57BL/6 mice, 6-10 weeks old were intradermally injected with 10µg of
413 LPS (Invivogen) to stimulate the right inguinal skin draining lymph node. Mice were euthanized
414 by CO_2 inhalation 1, 3, 5, 7, or 14 days after injection. Lymph nodes were collected and any fat
415 surrounding the tissue was removed. Tissues were then placed in cold 1x phosphate buffered saline
416 (PBS) with 2% fetal bovine serum (FBS, ThermoFisher). All animal work was approved by the
417 Institutional Animal Care and Use Committee.

418 **Flow cytometry**

419 After intradermal injection with LPS, inguinal lymph nodes were harvested for flow

420 cytometry analysis. A single cell suspension was collected by pushing lymph nodes through a 70
421 μm cell strainer and then resuspending in RPMI (ThermoFisher) supplemented with 10% FBS
422 (ThermoFisher), 1× l-glutamine (Corning), 50 U mL^{-1}Pen/Strep (Sigma), 50 μM beta-
423 mercaptoethanol (ThermoFisher), 1 mM sodium pyruvate (ThermoFisher), 1× nonessential amino
424 acids (Fisher Scientific), and 20 mM HEPES (GE Healthcare). Single cell suspensions were
425 stained for viability (live/dead), B cells (B220+), total T cells (CD3+), helper T cells (CD4+), and
426 cytotoxic T cells (CD8+). Stained cell suspensions were analyzed using flow cytometry with a BD
427 FACS Celesta and FlowJo Version 10.

428 **Tissue slicing**

429 Slicing of lymph nodes was done as previously described[30,32]. Briefly, tissues were
430 embedded in a 6% w/v low melting agarose (Thomas Scientific) and left to solidify. Once the gel
431 was solidified, tissues were punched out using a 10 mm biopsy punch (Robbins Instruments). Gel
432 pieces were placed on the sample tray of a Leica VT1000s vibratome (speed of 3.9 mm/s,
433 frequency of 0.3 Hz, and amplitude of 0.6 mm) and sliced 300 μm thick. Slices were collected
434 using a brush and placed into RPMI (ThermoFisher) supplemented with 10% FBS (ThermoFisher),
435 1× l-glutamine (Corning), 50 U mL^{-1}Pen/Strep (Sigma), 50 μM beta-mercaptoethanol
436 (ThermoFisher), 1 mM sodium pyruvate (ThermoFisher), 1× nonessential amino acids (Fisher
437 Scientific), and 20 mM HEPES (GE Healthcare). Lymph node slices were incubated at 37 °C with
438 5% CO_2 in media for at least 1 h prior to performing multiple particle tracking.

439 **Immunofluorescence staining**

440 Slices were stained for B and T cell zones as previous described[30]. Briefly, lymph nodes
441 were blocked with purified anti-mouse CD16/32 (BioLegend) and then stained for B cell or T cell
442 zones using primary and secondary antibodies: anti-mouse CD45R/B220-AF647 (BioLegend),

443 anti-collagen III (Proteintech), and donkey anti-rabbit 488 (BioLegend).

444 **Nanoparticle formulation**

445 500 nm polystyrene beads were densely coated in polyethylene glycol (PEG) using ethyl-
446 3-(3-dimethylaminopropyl) carbodiimide (EDC) and *N*-hydroxysuccinimide (NHS) chemistry, as
447 previously described[60]. Particles were diluted in deionized (DI) water at a 1:4 ratio and sonicated.
448 5 kDa or 40 kDa amine-terminated PEG (Creative PEGworks) were conjugated to the surface of
449 500 nm and 1 µm carboxylate-modified fluorescent polystyrene beads (Fluospheres™,
450 ThermoFisher), respectively, using 0.02 mM EDC (Invitrogen) and 14 mM NHS (Sigma)
451 dissolved in 200mM borate buffer (pH = 8.2). The reaction was allowed to proceed on a rotary
452 shaker for at least 4 hours at room temperature. For maximum PEG coverage on 500 nm and 1 µm
453 beads, 1.575 µmol of 5kDa PEG and 0.2175 µmol of 40kDa PEG were used, respectively. Particles
454 were centrifuged for 10 minutes at 15000 x g and 12 minutes at 10000 x g for 500 nm and 1 µm
455 particles, respectively, and washed 3 times using deionized (DI) water. Particles were resuspended
456 at 1% w/v in DI water and stored at 4ºC. Particle size and ζ-potential was characterized using
457 dynamic light scattering (DLS) and phase analysis light scattering (PALS) (Brookhaven
458 Instruments).

459 **Multiple particle tracking (MPT) analysis**

460 Up to 2 µL of a 1:1000 nanoparticle dilution was pipetted on top of each lymph node slice.
461 A coverslip was placed on top of the slice. A ZEISS Axioscope 5 microscope with 63X objective
462 using ZEISS software (ZEN lite) was used to capture videos at a temporal resolution of 30 ms for
463 10 seconds. Four slices were collected from each node, with 3 videos collected from each slice
464 (representing the B cell zone, T cell zone, and a random zone). Averages for the 'overall node' are
465 computed from data collected from all 4 slices across all zones (total of 12 videos per lymph node).

466 Averages for the B and T cell zones ignore all videos collected in the random zone. Ensemble
467 averaged mean square displacement (MSD) was calculated from nanoparticle trajectory using
468 MATLAB[61] with at least 50 particles per video. MSD was calculated using $\Delta r^2(\tau) = [x\ (t+\tau)$
469 $- x(t)]^2 + [y\ (t+\tau) - y(t)]^2$. The MSD values were then used to extrapolate the microrheological
470 properties of the tissue using the generalized Stokes-Einstein relation[33], defined as $\tilde{G}(s) =$
471 $\frac{k_B T}{\pi a s \langle \Delta r^2(s) \rangle}$, where k_BT is the thermal energy, a is the particle radius, and s is the complex Laplace
472 frequency. Using the frequency-dependent, complex modulus equation, $G^*(\omega) = G'(\omega) +$
473 $iG''(\omega)$, where s is substituted with $i\omega$, we can solve for the elastic and loss moduli. The complex
474 microviscosity (η^*) can be calculated as $\eta^* = G^*(\omega)/\omega$, where ω is the frequency. Comparisons
475 of loss and elastic moduli were made at a value of 1Hz, in line with standard rheological
476 measurements. The pore size (ξ) is estimated from the MSD[62] using the equation $\xi = \sqrt{MSD_{1s}} + a$,
477 where a is the particle radius. Pore size data represent all pore sizes collected from all particles in
478 each slice.

479 **Gap analysis**

480 Lymph nodes were embedded in optimal cutting temperature compound (Tissue-Tek
481 O.C.T. Compound) and flash frozen via liquid nitrogen. Tissues were stored at -80°C until slicing.
482 10 μm thick slices were collected using a Leica CM1950 Cryostat. Tissues were then washed with
483 1x PBS to remove excess OCT and fixed with 2% paraformaldehyde (PFA) in 1x PBS for 5-15
484 minutes. Tissues were blocked with 0.5% w/v casein in 1x PBS. Slices were imaged using a
485 FV3000 Laser Scanning Confocal Microscope (Olympus) with the following settings: 1.5x zoom
486 with 1024x1024 pixel resolution. The tiling feature was used to create a stitched 3x3 image of the
487 tissue. Z-stack images were captured with 10 slices, each separated by a 0.5-step interval. Images

488 were analyzed using FIJI. The individual stacks were merged using the z-project function at
489 standard deviation projection. Images were then processed using the Gap analysis script[7]. Briefly,
490 images were resized by a factor of 0.4. They were then converted into binary based on a pixel
491 intensity threshold of 0.001. The largest circles possible were fitted into the gaps so that the circles
492 were not overlapping with each other. Circle radii were collected in pixels and converted to μm
493 based on the microscope resolution using the Gap analysis script.

494 **Statistics**

495 All statistical analyses were performed using GraphPad Prism 10. P values ≤ 0.05 are
496 considered significant. Sample sizes were predetermined based on power analysis ($p=0.05$, $\alpha =$
497 0.8) and guided by prior experience with similar experiments. In general, two-group comparisons
498 were performed using two-tailed, unpaired Student's t-tests or their non-parametric equivalents
499 depending on data distribution. For multiple group comparisons, one-way ANOVA with Tukey's
500 multiple comparison test or a non-parametric Kruskal-Wallis test followed by Dunn's multiple
501 comparisons test were conducted. Normality and homoscedasticity were evaluated prior to
502 analysis to confirm the assumptions of the statistical tests applied. Figure legends include details
503 of the statistical analyses performed for the figure dataset.

504 **ACKNOWLEDGEMENTS**

505 This work was supported by financial support from NIGMS MIRA 1R35GM142835-01 (KM, VS)
506 and NIH HPI T32 (AR). All animal procedures were performed in accordance with the Guide for
507 the Care and Use of Laboratory Animals and the American Veterinary Medical Association
508 (AVMA) Guidelines for the Euthanasia of Animals and approved by the Institutional Animal Care
509 and Use Committee at the University of Maryland, College Park. We would like to thank
510 Dr. Giuliano Scarcelli, Sachin Suresh, and Anoushka Dasgupta for their inputs on the analysis.

511 **LIST OF ABBREVIATIONS**

512 ECM – Extracellular Matrix

513 FRC – Fibroblastic Reticular Cell

514 MPT – Multiple Particle Tracking

515 DC – Dendritic Cell

516 LPS - Lipopolysaccharide

517 MFI – Mean Fluorescence Intensity

518 TLR - Toll-like Receptor

519 PEG - Polyethylene glycol

520 DI - Deionized

521 EDC - Ethyl-3-(3-dimethylaminopropyl) carbodiimide

522 NHS - *N*-hydroxysuccinimide

523 DLS – Dynamic Light Scattering

524 PALS – Phase Analysis Light Scattering

525 MSD – Mean Square Displacement

526 OCT – Optimal Cutting Temperature

527 PFA – Paraformaldehyde

528 PBS – Phosphate Buffered Saline

REFERENCES

1. Schudel, A., Francis, D. M. & Thomas, S. N. Material design for lymph node drug delivery. *Nat Rev Mater* **4**, 415-428, doi:10.1038/s41578-019-0110-7 (2019).
2. Li, L., Wu, J., Abdi, R., Jewell, C. M. & Bromberg, J. S. Lymph node fibroblastic reticular cells steer immune responses. *Trends Immunol.* **42**, 723-734, doi:10.1016/j.it.2021.06.006 (2021).
3. Fletcher, A. L., Acton, S. E. & Knoblich, K. Lymph node fibroblastic reticular cells in health and disease. *Nat. Rev. Immunol.* **15**, 350-361, doi:10.1038/nri3846 (2015).
4. Yang, C.-Y. *et al.* Trapping of naive lymphocytes triggers rapid growth and remodeling of the fibroblast network in reactive murine lymph nodes. *Proceedings of the National Academy of Sciences* **111**, E109-E118, doi:doi:10.1073/pnas.1312585111 (2014).
5. Zhu, M. & Fu, Y.-X. The role of core TNF/LIGHT family members in lymph node homeostasis and remodeling. *Immunol. Rev.* **244**, 75-84, doi:https://doi.org/10.1111/j.1600-065X.2011.01061.x (2011).
6. Astarita, J. L. *et al.* The CLEC-2-podoplanin axis controls the contractility of fibroblastic reticular cells and lymph node microarchitecture. *Nat. Immunol.* **16**, 75-84, doi:10.1038/ni.3035 (2015).
7. Acton, S. E. *et al.* Dendritic cells control fibroblastic reticular network tension and lymph node expansion. *Nature* **514**, 498-502, doi:10.1038/nature13814 (2014).
8. Horsnell, H. L. *et al.* Lymph node homeostasis and adaptation to immune challenge resolved by fibroblast network mechanics. *Nat. Immunol.* **23**, 1169-1182, doi:10.1038/s41590-022-01272-5 (2022).
9. Assen, F. P. *et al.* Multitier mechanics control stromal adaptations in the swelling lymph node. *Nat. Immunol.* **23**, 1246-1255, doi:10.1038/s41590-022-01257-4 (2022).
10. Alapan, Y. & Thomas, S. N. Mechanics drive lymph node expansion. *Nat. Immunol.* **23**, 1139-1141, doi:10.1038/s41590-022-01277-0 (2022).
11. Martinez, V. G. *et al.* Fibroblastic Reticular Cells Control Conduit Matrix Deposition during Lymph Node Expansion. *Cell Rep.* **29**, 2810-2822.e2815, doi:https://doi.org/10.1016/j.celrep.2019.10.103 (2019).
12. Textor, J., Mandl, J. N. & de Boer, R. J. The Reticular Cell Network: A Robust Backbone for Immune Responses. *PLoS Biol.* **14**, e2000827, doi:10.1371/journal.pbio.2000827 (2016).
13. Bajénoff, M. *et al.* Stromal cell networks regulate lymphocyte entry, migration, and territoriality in lymph nodes. *Immunity* **25**, 989-1001, doi:10.1016/j.immuni.2006.10.011 (2006).
14. Lämmermann, T. & Sixt, M. The microanatomy of T-cell responses. *Immunol. Rev.* **221**, 26-43, doi:https://doi.org/10.1111/j.1600-065X.2008.00592.x (2008).
15. Roozendaal, R., Mebius, R. E. & Kraal, G. The conduit system of the lymph node. *Int. Immunol.* **20**, 1483-1487, doi:10.1093/intimm/dxn110 (2008).
16. Adu-Berchie, K. *et al.* Generation of functionally distinct T-cell populations by altering the viscoelasticity of their extracellular matrix. *Nat Biomed Eng* **7**, 1374-1391, doi:10.1038/s41551-023-01052-y (2023).
17. Kwok, T. *et al.* Age-Associated Changes to Lymph Node Fibroblastic Reticular Cells. *Frontiers in Aging* **3**, doi:10.3389/fragi.2022.838943 (2022).
18. Sonar, S. A. *et al.* Early age–related atrophy of cutaneous lymph nodes precipitates an early

functional decline in skin immunity in mice with aging. *Proceedings of the National Academy of Sciences* **119**, e2121028119, doi:10.1073/pnas.2121028119 (2022).

19. Chaudhuri, O., Cooper-White, J., Janmey, P. A., Mooney, D. J. & Shenoy, V. B. Effects of extracellular matrix viscoelasticity on cellular behaviour. *Nature* **584**, 535-546, doi:10.1038/s41586-020-2612-2 (2020).
20. Batzdorf, C. S. *et al.* Sexual Dimorphism in Extracellular Matrix Composition and Viscoelasticity of the Healthy and Inflamed Mouse Brain. *Biology (Basel)* **11**, doi:10.3390/biology11020230 (2022).
21. Simon, L. R., Scott, A. J., Figueroa Rios, L., Zembles, J. & Masters, K. S. Cellular-scale sex differences in extracellular matrix remodeling by valvular interstitial cells. *Heart Vessels* **38**, 122-130, doi:10.1007/s00380-022-02164-2 (2023).
22. Guo, J. *et al.* Brain maturation is associated with increasing tissue stiffness and decreasing tissue fluidity. *Acta Biomater.* **99**, 433-442, doi:10.1016/j.actbio.2019.08.036 (2019).
23. Hernandez, P. A. *et al.* Sexual Dimorphism in the Extracellular and Pericellular Matrix of Articular Cartilage. *Cartilage* **13**, 19476035221121792, doi:10.1177/19476035221121792 (2022).
24. Ricarte, R. G. & Shanbhag, S. A tutorial review of linear rheology for polymer chemists: basics and best practices for covalent adaptable networks. *Polymer Chemistry* **15**, 815-846, doi:10.1039/D3PY01367G (2024).
25. Cho, D. H., Aguayo, S. & Cartagena-Rivera, A. X. Atomic force microscopy-mediated mechanobiological profiling of complex human tissues. *Biomaterials* **303**, 122389, doi:https://doi.org/10.1016/j.biomaterials.2023.122389 (2023).
26. Krieg, M. *et al.* Atomic force microscopy-based mechanobiology. *Nature Reviews Physics* **1**, doi:10.1038/s42254-018-0001-7 (2018).
27. Fonta, C. M. *et al.* Fibronectin fibers are highly tensed in healthy organs in contrast to tumors and virus-infected lymph nodes. *Matrix Biol Plus* **8**, 100046, doi:10.1016/j.mbplus.2020.100046 (2020).
28. Lobov, G. I. & Pan'kova, M. N. Mechanical Properties of Lymph Node Capsule. *Bull. Exp. Biol. Med.* **151**, 5-8, doi:10.1007/s10517-011-1246-7 (2011).
29. Najibi, A. J. *et al.* Lymph node expansion predicts magnitude of vaccine immune response. *bioRxiv*, 2022.2010.2025.513749, doi:10.1101/2022.10.25.513749 (2022).
30. Ramirez, A., Merwitz, B., Lee, H., Vaughan, E. & Maisel, K. Multiple particle tracking (MPT) using PEGylated nanoparticles reveals heterogeneity within murine lymph nodes and between lymph nodes at different locations. *Biomater Sci* **10**, 6992-7003, doi:10.1039/d2bm00816e (2022).
31. Lee, B., Cheema, Y., Bader, S. & Duncan, G. *Shaping nanoparticle diffusion through biological barriers to drug delivery*. (2021).
32. Belanger, M. C. *et al.* Acute Lymph Node Slices Are a Functional Model System to Study Immunity Ex Vivo. *ACS Pharmacology & Translational Science* **4**, 128-142, doi:10.1021/acsptsci.0c00143 (2021).
33. Mason, T. G. & Weitz, D. A. Optical Measurements of Frequency-Dependent Linear Viscoelastic Moduli of Complex Fluids. *Phys. Rev. Lett.* **74**, 1250-1253, doi:10.1103/PhysRevLett.74.1250 (1995).
34. Ensign, L. M. *et al.* Ex Vivo Characterization of Particle Transport in Mucus Secretions Coating Freshly Excised Mucosal Tissues. *Mol. Pharm.* **10**, 2176-2182, doi:10.1021/mp400087y (2013).

35. McCright, J., Skeen, C., Yarmovsky, J. & Maisel, K. Nanoparticles with dense poly(ethylene glycol) coatings with near neutral charge are maximally transported across lymphatics and to the lymph nodes. *Acta Biomater.*, doi:https://doi.org/10.1016/j.actbio.2022.03.054 (2022).
36. McGlynn, J. A., Wu, N. & Schultz, K. M. Multiple particle tracking microrheological characterization: Fundamentals, emerging techniques and applications. *Journal of Applied Physics* **127**, 201101, doi:10.1063/5.0006122 (2020).
37. Du, H. *et al.* Tuning immunity through tissue mechanotransduction. *Nature Reviews Immunology* **23**, 174-188, doi:10.1038/s41577-022-00761-w (2023).
38. Huse, M. Mechanical forces in the immune system. *Nat. Rev. Immunol.* **17**, 679-690, doi:10.1038/nri.2017.74 (2017).
39. Gunasinghe, S. D., Peres, N. G., Goyette, J. & Gaus, K. Biomechanics of T Cell Dysfunctions in Chronic Diseases. *Front. Immunol.* **12**, doi:10.3389/fimmu.2021.600829 (2021).
40. Link, A. *et al.* Fibroblastic reticular cells in lymph nodes regulate the homeostasis of naive T cells. *Nat. Immunol.* **8**, 1255-1265, doi:10.1038/ni1513 (2007).
41. Kumar, V. *et al.* A dendritic-cell-stromal axis maintains immune responses in lymph nodes. *Immunity* **42**, 719-730, doi:10.1016/j.immuni.2015.03.015 (2015).
42. Yamada, K. M. & Sixt, M. Mechanisms of 3D cell migration. *Nature Reviews Molecular Cell Biology* **20**, 738-752, doi:10.1038/s41580-019-0172-9 (2019).
43. Swift, J. *et al.* Nuclear lamin-A scales with tissue stiffness and enhances matrix-directed differentiation. *Science* **341**, 1240104, doi:10.1126/science.1240104 (2013).
44. Harada, T. *et al.* Nuclear lamin stiffness is a barrier to 3D migration, but softness can limit survival. *J. Cell Biol.* **204**, 669-682, doi:10.1083/jcb.201308029 (2014).
45. Song, J. *et al.* The extracellular matrix of lymph node reticular fibres modulates follicle border interactions and germinal centre formation. *iScience* **26**, 106753, doi:10.1016/j.isci.2023.106753 (2023).
46. Klein, S. L. & Flanagan, K. L. Sex differences in immune responses. *Nature Reviews Immunology* **16**, 626-638, doi:10.1038/nri.2016.90 (2016).
47. Sonia Sharma et al., Sex differences in tissue-specific immunity and immunology.Science389,599-603(2025). DOI:10.1126/science.adx4381
48. Takahashi, T. *et al.* Sex differences in immune responses that underlie COVID-19 disease outcomes. *Nature* **588**, 315-320, doi:10.1038/s41586-020-2700-3 (2020).
49. Aomatsu, M., Kato, T., Kasahara, E. & Kitagawa, S. Gender difference in tumor necrosis factor-α production in human neutrophils stimulated by lipopolysaccharide and interferon-γ. *Biochem. Biophys. Res. Commun.* **441**, 220-225, doi:10.1016/j.bbrc.2013.10.042 (2013).
50. Asai, K. *et al.* Gender differences in cytokine secretion by human peripheral blood mononuclear cells: role of estrogen in modulating LPS-induced cytokine secretion in an ex vivo septic model. *Shock* **16**, 340-343, doi:10.1097/00024382-200116050-00003 (2001).
51. Campesi, I., Montella, A. & Franconi, F. Human monocytes respond to lipopolysaccharide (LPS) stimulation in a sex-dependent manner. *J. Cell. Physiol.* **237**, 580-588, doi:10.1002/jcp.30503 (2022).
52. Aulock, S. V. *et al.* Gender difference in cytokine secretion on immune stimulation with LPS and LTA. *J. Interferon Cytokine Res.* **26**, 887-892, doi:10.1089/jir.2006.26.887 (2006).
53. Musabak, U. *et al.* Gonadotropin treatment restores in vitro interleukin-1beta and tumour

necrosis factor-alpha production by stimulated peripheral blood mononuclear cells from patients with idiopathic hypogonadotropic hypogonadism. *Clin. Exp. Immunol.* **132**, 265-270, doi:10.1046/j.1365-2249.2003.02141.x (2003).

54. D'Agostino, P. *et al.* Sex hormones modulate inflammatory mediators produced by macrophages. *Ann. N. Y. Acad. Sci.* **876**, 426-429, doi:10.1111/j.1749-6632.1999.tb07667.x (1999).
55. Rettew, J. A., Huet-Hudson, Y. M. & Marriott, I. Testosterone reduces macrophage expression in the mouse of toll-like receptor 4, a trigger for inflammation and innate immunity. *Biol. Reprod.* **78**, 432-437, doi:10.1095/biolreprod.107.063545 (2008).
56. Chi, L. *et al.* Sexual dimorphism in skin immunity is mediated by an androgen-ILC2-dendritic cell axis. *Science* **384**, eadk6200, doi:10.1126/science.adk6200 (2024).
57. Gubbels Bupp, M. R. Sex, the aging immune system, and chronic disease. *Cell. Immunol.* **294**, 102-110, doi:https://doi.org/10.1016/j.cellimm.2015.02.002 (2015).
58. Nikolich-Žugich, J. The twilight of immunity: emerging concepts in aging of the immune system. *Nat. Immunol.* **19**, 10-19, doi:10.1038/s41590-017-0006-x (2018).
59. Cakala-Jakimowicz, M., Kolodziej-Wojnar, P. & Puzianowska-Kuznicka, M. Aging-Related Cellular, Structural and Functional Changes in the Lymph Nodes: A Significant Component of Immunosenescence? An Overview. *Cells* **10**, 3148 (2021).
60. Nance, E. A. *et al.* A Dense Poly(Ethylene Glycol) Coating Improves Penetration of Large Polymeric Nanoparticles Within Brain Tissue. *Sci. Transl. Med.* **4**, 149ra119-149ra119, doi:10.1126/scitranslmed.3003594 (2012).
61. Schuster, B. S., Suk, J. S., Woodworth, G. F. & Hanes, J. Nanoparticle diffusion in respiratory mucus from humans without lung disease. *Biomaterials* **34**, 3439-3446,://doi.org/10.1016/j.biomaterials.2013.01.064 (2013).
62. Shin, J. H., Gardel, M. L., Mahadevan, L., Matsudaira, P. & Weitz, D. A. Relating microstructure to rheology of a bundled and cross-linked F-actin network in vitro. *Proc. Natl. Acad. Sci. U. S. A.* **101**, 9636-9641, doi:10.1073/pnas.0308733101 (2004).
63. Cabral, Jaydee, and Stephen Carl Moratti. "Hydrogels for biomedical applications." *Future medicinal chemistry* vol. 3,15 (2011): 1877-88. doi:10.4155/fmc.11.134
64. Q. L. Loh and C. Choong, Three-dimensional scaffolds for tissue engineering applications: role of porosity and pore size, Tissue Eng., Part B, 2013, 19(6), 485–502.
65. Hoffman AS. Hydrogels for biomedical applications. *Adv Drug Deliv Rev*. 2002;54(1):3-12
66. Leal-Egaña, Aldo et al. "Determination of pore size distribution at the cell-hydrogel interface." *Journal of nanobiotechnology* vol. 9 24. 27 May. 2011, doi:10.1186/1477-3155-9-24
67. Bernardette Martínez-Rizo, Abril et al. "Models in vivo and in vitro for the study of acute and chronic inflammatory activity: A comprehensive review." *International immunopharmacology* vol. 135 (2024): 112292. doi:10.1016/j.intimp.2024.112292
68. Rafiyan M, Sadeghmousavi S, Akbarzadeh M, Rezaei N. Experimental animal models of chronic inflammation. *Curr Res Immunol*. 2023;4:100063. Published 2023 Jun 11. doi:10.1016/j.crimmu.2023.100063
69. Katherine Joyner, Sydney Yang, Gregg A. Duncan; Microrheology for biomaterial design. *APL Bioeng.* 1 December 2020; 4 (4): 041508. https://doi.org/10.1063/5.0013707
70. Mao Y, Nielsen P and Ali J (2022) Passive and Active Microrheology for Biomedical Systems. Front. Bioeng. Biotechnol. 10:916354. doi: 10.3389/fbioe.2022.916354

712 71. Wirtz, D. (2009). Particle-tracking microrheology of living cells: principles and
713 applications. *Annual review of biophysics*, *38*(1), 301-326
714 72. He X, Yang Y, Han Y, Cao C, Zhang Z, Li L, Xiao C, Guo H, Wang L, Han L, Qu Z, Liu
715 N, Han S, Xu F. Extracellular matrix physical properties govern the diffusion of
716 nanoparticles in tumor microenvironment. Proc Natl Acad Sci U S A.
717 2023;120(1):e2209260120. doi:10.1073/pnas.2209260120.